ACS APPLIED MATERIALS & INTERFACES

Research Article

www.acsami.org

MoO_2/Multiwalled Carbon Nanotubes (MWCNT) Hybrid for Use as a Li-Ion Battery Anode

Akkisetty Bhaskar,[†] Melepurath Deepa,*[,‡] and Tata Narasinga Rao[§]

[†]Department of Materials Science and Engineering and [‡]Department of Chemistry, Indian Institute of Technology Hyderabad, Ordnance Factory Estate, Yeddumailaram 502205, Andhra Pradesh, India

[§]Nanomaterials Center, International Advanced Research Centre for Powder Metallurgy and New Materials (ARCI), Hyderabad 500005, India

Supporting Information

ABSTRACT: A molybdenum dioxide/multiwalled carbon nanotubes (MoO_2/MWCNT) hybrid composed of spherical flowerlike nanostructures of MoO_2, interconnected by MWCNTs has been prepared by a one-step hydrothermal route. The growth of MoO_2 nanoparticles into spherical floral shapes with a monoclinic crystalline structure is steered by the dioctyl sulfosuccinate surfactant. The one-dimensional electron transport pathways provided by MWCNTs, which are in direct contact with MoO_2 nanostructures, impart an enhanced reversible lithium storage capacity (1143 mA h g^{-1} at a current density of 100 mA g^{-1} after 200 cycles), high rate capability (408 mA h g^{-1} at a high C-rate of 1000 mA g^{-1}) and good cycling stability to the MoO_2/MWCNT hybrid relative to neat MoO_2. Surface potential mapping of the electrodes by Kelvin probe force microscopy, revealed a lower localized work function for the MoO_2/MWCNT hybrid as compared to the neat oxide. This makes the MoO_2/MWCNT hybrid more easily oxidizable than neat MoO_2. Such a distinctive topology achieved for the MoO_2/MWCNT hybrid, wherein the MWCNTs prevent the agglomeration of MoO_2 nanostructures and thus preserve good electrical connectivities, makes it different in terms of both morphology and performance from all previously reported MoO_2-based anode materials to date.

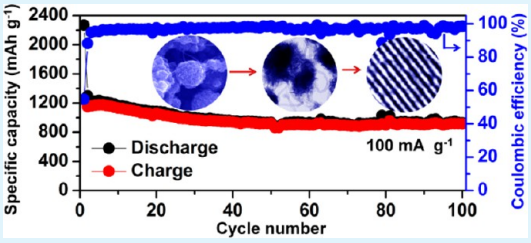

KEYWORDS: *anode, charge−discharge, lithium ion batteries, molybdenum dioxide, multiwalled carbon nanotubes*

1. INTRODUCTION

The ever-increasing global warming due to gaseous emissions and the burgeoning fuel costs have escalated the search for viable energy efficient alternatives such as electric-powered vehicles. The Li-ion battery is now universally accepted as an electrical energy storage device that can offer the best energy-to-weight performance, especially in view of portable applications. Although extensive research efforts have been devoted to the development of various anodes, cathodes, and electrolyte materials,[1−3] but the enormous demand for Li-ion batteries capable of delivering high energy density along with long cyclability provides the impetus to synthesize high performance electrode materials. In the commercially available Li-ion batteries, the anode material is typically graphite, which is characterized by a rather low theoretical specific capacity of 374 mA h g^{-1}.[4,5] The low capacity of the anode material limits the performance of battery. In the past, graphite has been successfully replaced by transition metal oxides like iron oxide, cobalt oxide, nickel oxide, etc.[6] The oxides can react with more than 2 lithiums per formula unit, through a conversion mechanism which effectively results in capacities higher than that delivered by graphite. But the slow diffusion kinetics in metal oxides acts to restrict their capacities.[7] Another shortcoming is that during charge−discharge, metal oxides undergo huge volume variation which eventually leads to the detachment of the active material from the current collector. To alleviate these issues, nanostructured forms of metal oxides[4,8] and carbon (in the form of polymers, carbon nanotubes and graphene) coated metal oxides[9−11] have been used by researchers as anodes for Li-ion batteries.

Among anode materials, molybdenum oxide (MoO_2) is particularly attractive, as it offers an extremely large theoretical specific capacity of ∼840 mA g^{-1}, corresponding to an insertion of 4 lithiums. To date, there are several reports on MoO_2 with different nanostructures which include mesoporous, nanowires, nanorods, and tremella like shapes.[12−15] In addition, the performances of MoO_2/C and MoO_2/graphene composites as anodes have also been investigated.[16−21] For instance, MoO_2 nanowires prepared by Gao and co-workers showed an initial capacity of 595.7 mA h g^{-1} at a current density of 200 mA g^{-1} and at the end of 20 cycles, a capacity of ∼500 mA h g^{-1} was retained.[13] Shi et. al's report revealed the ability of mesoporous MoO_2 to deliver a reversible capacity of 630 mA h g^{-1} which increased to a value of 750 mA h g^{-1} after 30 cycles. But this capacity was achieved at a rather low C-rate of 0.05.[12] In another study on ultrafine MoO_2 nanorods, 5 nm in diameter, an initial reversible capacity of 521 mA h g^{-1} was reported and it gradually reached a value of 830 mA h g^{-1} after 30 cycles, but

Received: December 18, 2012
Accepted: March 12, 2013
Published: March 12, 2013

again, at a very low *C*-rate of 0.05.[14] Tremella-like structured MoO_2 prepared by Yang et. al, showed an initial reversible capacity of 538.0 mA h g^{-1} at a current density of 0.5 mA cm^{-2} and the capacity rose to 650 mA h g^{-1} in the subsequent cycles.[15] For a composite of ultrafine MoO_2 nanoparticles distributed homogeneously in a carbon matrix,[17] authors found that it exhibited a stable capacity of ∼602 mA h g^{-1} for ∼600 cycles at a current density of 100 mA g^{-1}. In our previous study on a MoO_2 nanoparticle composite with graphene, an initial capacity of 703.7 mA h g^{-1} was obtained and it faded to 530 mA h g^{-1} at the end 1000 cycles, at a current density of 540 mA h g^{-1}.[19] It is apparent that MoO_2 composites with novel nanoscale architectures that can deliver high rate capability, capacity, and cyclability are desirable.

To the best of our knowledge, the use of a MoO_2/MWCNT hybrid as an anode in a Li ion battery has not been reported till date. Since MWCNTs are bestowed with one-dimensional tubular structures, high electrical and thermal conductivities,[22] and large surface areas,[23] they are ideal for combining with MoO_2. Moreover, the synergy between the functions of the two materials, high capacity of MoO_2, and good electronic conductivity and large surface area of MWCNTs can be exploited in the MoO_2/MWCNT hybrid to yield high-performance anodes in Li-ion batteries. It is well-known that CNTs are highly hydrophobic and the surface should be functionalized for dispersing in an aqueous medium. CNTs can be functionalized in two different ways one is covalent (by use of an acid) and other is noncovalent (by adsorption of a base like poly(diallyldimethylammonium chloride). The noncovalent method is preferred over covalent method because the surface property as well as electronic conductivity is not disturbed.[24−27] On the basis of previous studies, one frequently used approach for increasing the dispersibility of CNTs is noncovalent modification using a surfactant. This is because of the simplicity of the procedures involved, such as ultrasonication and centrifugation or filtration, along with a capacity for preserving the nanotube structures and properties. In this context, an anionic surfactant like sodium dioctyl sulfosuccinate (AOT) has been used to solubilize and debundle single walled carbon nanotubes (SWCNTs) in aqueous solution via noncovalent interactions.[24−27] Heretofore unreported, we present an easy single-step synthesis of MoO_2/MWCNT hybrid by hydrothermal method. We used AOT, which not only served as a reducing agent for Mo salt reduction but also tailored the growth of MoO_2 nanoparticles into three-dimensional spherical shaped flowerlike morphologies. In addition, AOT also aids in dispersing MWCNTs. High resolution transmission electron microscopy (HRTEM) and X-ray diffraction (XRD) studies gave insights to the microstructural features of MoO_2/MWCNT hybrid and the neat materials (MoO_2 and MWCNTs). For the first time, we also followed the energetics of the system, by use of Kelvin probe force microscopy (KPFM) and how it can impact battery performance. We evaluated in detail, the electrochemical characteristics of the MoO_2/MWCNT hybrid by incorporating it as the working electrode in a Li-ion battery configuration and correlated the outstanding performance attributes with the unique morphology of this anode material.

2. EXPERIMENTAL SECTION

2.1. Materials. All of the reactants were of analytical grade and used without further purification. Ammonium heptamolybdate tetrahydrate (AHM) and battery electrolyte: 1 M $LiPF_6$ dissolved in a mixture of ethylene carbonate (EC) and dimethyl carbonate (DMC) (1:1 v/v) were purchased from Merck. AOT and MWCNTs were purchased from Sigma-Aldrich. Lithium foil was purchased from Alfa-Aesar. MWCNTs were purified by ultrasonic treatment in 6 M nitric acid for 0.5 h and then refluxing in 2.6 M HNO_3 solution for 36 h before use. Ultrapure water (resistivity ≈ 18.2 MΩ cm) obtained through Millipore Direct-Q3 UV system was used as solvent.

2.2. Synthesis of the MoO_2/MWCNT Hybrid. The MoO_2/MWCNT hybrid was prepared by a hydrothermal method using AOT as the surfactant. The first step involves the preparation of surface modified MWCNTs with AOT as surfactant. Typically, 100 mg of MWCNTs were added to 20 mL of absolute ethanol and ultrasonicated for 0.5 h. To this suspension, 2 g of AOT dissolved in 15 mL of cyclohexane was added and the resulting mixture was ultrasonicated again for 0.5 h and stirred for 15 min and it formed a well-dispersed and homogeneous solution of MWCNTs. In a separate beaker, 0.5 mmol ammonium heptamolybdate tetrahydrate (AHM) was dissolved in 20 mL of ultrapure water and added to the above solution. This was followed by continuous stirring for 1 h at 25 °C. The resultant black colored solution was placed in a 100 mL Teflon lined autoclave and heated in an oven at 200 °C for 36 h. A black colored precipitate was obtained, and it was filtered and washed with ultrapure water followed by n-hexane. The resultant black powder was dried in a vacuum oven at 80 °C for 12 h and the dried MoO_2/MWCNT hybrid was stored in a glovebox. Neat MoO_2 was also prepared by following the same steps, but without adding MWCNTs. The optimization of the amount of surfactant (AOT) for producing MoO_2 flower like nanostructures, was accomplished by preparing neat MoO_2 by varying the concentration of AOT: by using 0.3, 0.6, 1, and 3 g of AOT, whereas all other experimental conditions were kept constant.

Working electrodes were prepared by mixing 80 wt % active material (MoO_2 or MoO_2/MWCNT hybrid), 10 wt % acetylene black and 10 wt % poly(vinylidene fluoride) with a few drops of N-methyl pyrrolidine. The resultant slurry in each case was coated on 13 mm stainless steel foils and dried at 80 °C for 12 h in vacuum oven for removing the solvent. Swagelok cells were employed for electrochemical measurements and these were assembled inside an argon filled glovebox (O_2 and H_2O concentration ≤1 ppm and 0.5 ppm). A lithium foil was used as a counter/reference electrode and a Whatman glass microfiber filter paper functioned as the separator. The electrolyte was 1 M $LiPF_6$ in EC:DMC (1:1 v/v). The electrodes referred to as neat MoO_2 and MoO_2/MWCNT hybrid in this report have been prepared from a solution based on 2 g AOT (200 °C for 36 h). For neat MoO_2, the same experimental conditions apply, unless specified otherwise.

2.3. Characterization Techniques. XRD on the electrodes was performed on PANalytical, X'PertPRO instrument with Cu K_α-radiation. A Bruker Senterra dispersive micro Raman spectrometer with a 532 nm laser was used for recording Raman spectra. Structural characterization was carried out by HRTEM (JEOL 3010 200 KV). For HRTEM, the sample was ultrasonicated for 0.5 h and carefully extracted onto a carbon-coated copper grid. Surface morphology analysis was performed on a Carl Zeiss (Supra 40) field emission scanning electron microscope (FE-SEM). Brunauer−Emmett−Teller (BET) specific surface area measurement was performed on Micromeritics, ASAP 2020. X-ray photoelectron spectroscopy (XPS, Omicron UK ESCA+) with AlK_α monochromatic X-ray radiation was used for the determination of chemical composition. KPFM (Veeco, Multimode 8 with ScanAsyst) was used for recording successive topography and surface potential images in taping mode (for details, see the Supporting Information). Thermal analysis of the electrode materials was accomplished on a TA Instruments Q600. Galvanostatic charge−discharge measurements were performed on a battery testing unit (Arbin Instruments, BT 2000) at different current densities in the range of 0.01 − 3 V versus Li/Li^+ at room temperature. Cyclic voltammetry (CV) and electrochemical impedance spectroscopy (EIS) measurements (100 kHz to 10 MHz, ac amplitude: 0.01 V) on the electrodes were performed on an Autolab PGSTAT 302N workstation.

3. RESULTS AND DISCUSSIONS

3.1. Characterization of Structure and Morphology. The XRD patterns of hydrothermally synthesized MoO_2 by heating at 200 °C for 36 h for various proportions of AOT (in the precursor solution) are shown in Figure 1. The XRD patterns of neat MoO_2 prepared with 0.3, 0.6, 1, and 2 g AOT surfactant show distinct peaks corresponding to the monoclinic structure of MoO_2 with space group of P21/c(14) (PCPDF NO: 860135). The field-emission scanning electron microscopy (FE-SEM) images of these materials are shown in Figure 2. The morphology of MoO_2 prepared from a 0.3 g AOT formulation shows compactly packed interconnected irregular shaped particles (Figure 2a). On increasing the AOT proportion to 0.6 g (Figure 2b), the image shows MoO_2 growing into bundles of randomly oriented stubs, around 120 nm in length and 35–50 nm in diameter. At 1 g AOT content, the SEM image shows that the MoO_2 stubs evolve into MoO_2 flakes (Figure 2c). At 2 g of AOT, the flakes evolve into a flower like morphology, which is advantageous for ion insertion/extraction during the discharge/charge process (Figure 2d). The high magnification image clearly shows the sheet like-shapes (Figure 2e) which organize into flowerlike structures. Upon raising the AOT content further to 3 g (Figure 2f), we observed that the same nanosheet like morphology was retained, indicating that 2 g of AOT is sufficient to induce the formation of flower like shapes encompassing the flaky sheets. Therefore we used the precursor

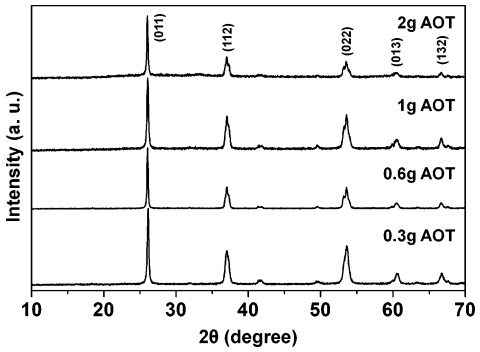

Figure 1. XRD patterns of neat MoO_2 prepared from solutions containing 0.3, 0.6, 1, and 2 g of AOT (by heating hydrothermally at 200 °C for 36 h).

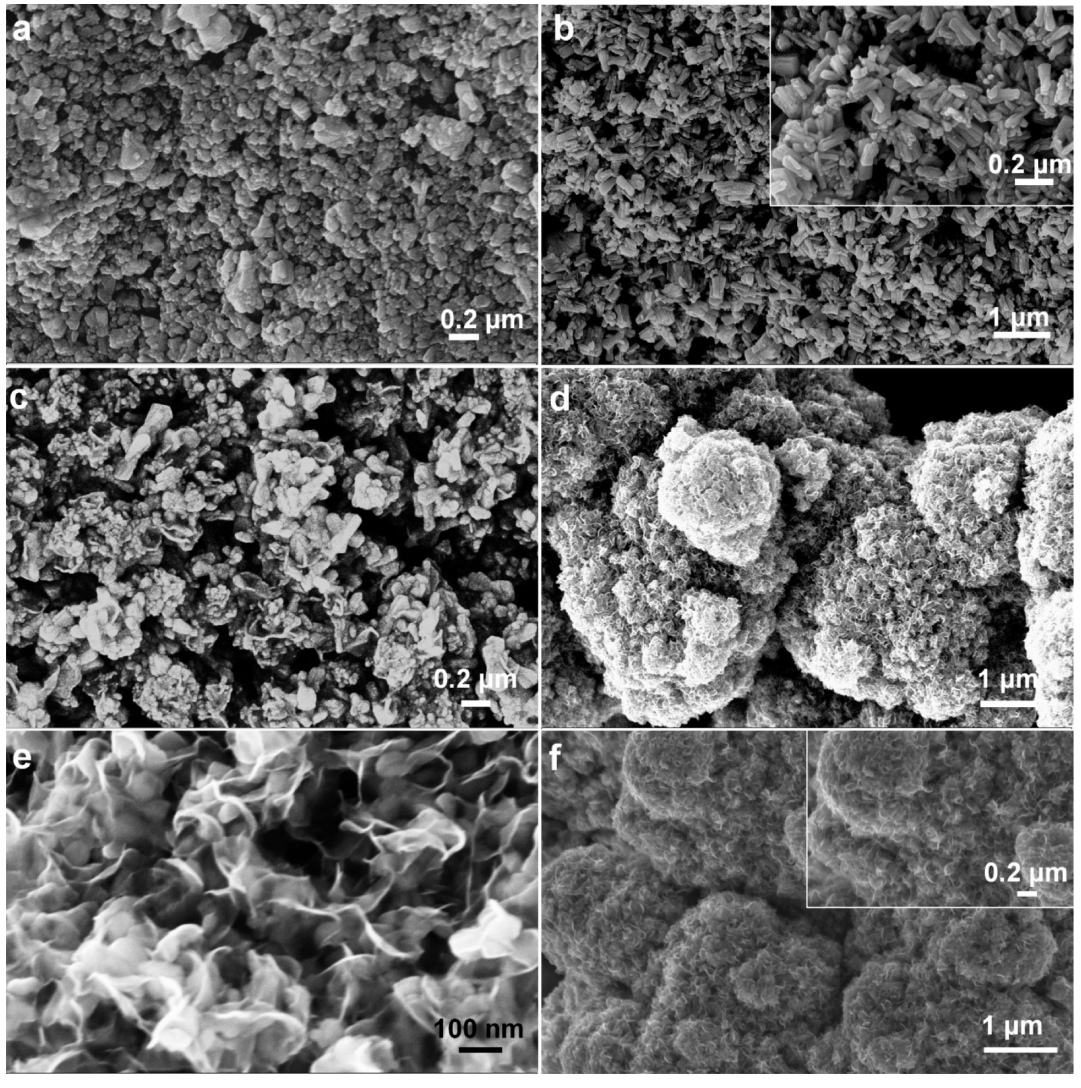

Figure 2. FE-SEM images of MoO_2 prepared from solutions containing (a) 0.3 (b) 0.6 (c) 1 (d, e) 2, and (f) 3 g of AOT (by hydrothermal heating at 200 °C for 36 h).

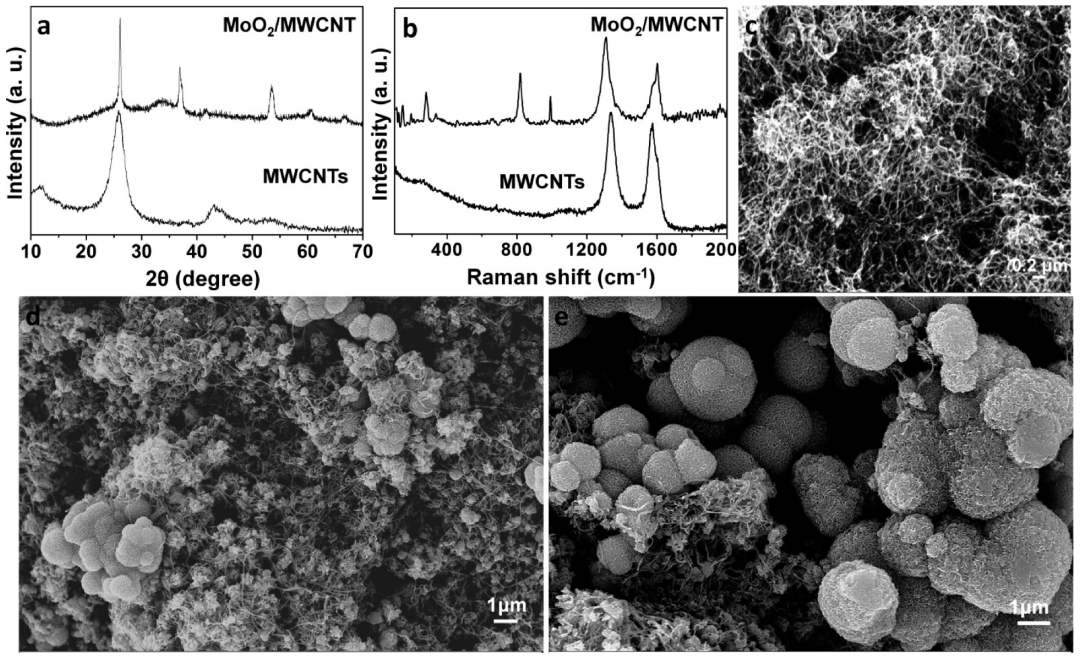

Figure 3. (a) XRD patterns and (b) Raman spectra of neat MWCNTs and the MoO_2/MWCNT hybrid. FE-SEM images of (c) neat MWCNTs and (d, e) MoO_2/MWCNT hybrid.

composition with 2 g of AOT for preparing the hybrid with MWCNTs.

The XRD patterns of the as-synthesized MoO_2/MWCNT hybrid (based on 2 g of AOT, 200 °C for 36 h) and MWCNTs are shown in Figure 3a. XRD patterns of the MoO_2/MWCNT hybrid can be readily indexed with monoclinic MoO_2 with a space group of P21/c(14) (PCPDF NO: 860135). The diffraction peaks at d = 3.4256, 2.4339, 2.1797, 1.7146, 1.5322, and 1.4017 Å correspond to (011), (112), (212), (022), (013), and (132) reflections of monoclinic MoO_2, respectively. The XRD pattern of neat MWCNTs shows a broad peak at d = 3.423 Å (2θ = 26.01°) which corresponds to (002) reflection. The Raman spectrum of neat MWCNTs and MoO_2/MWCNT hybrid are shown in Figure 3b. While the Raman spectrum of neat MWCNTs shows only the D and the G bands in the 1300−1600 cm^{-1} wavenumber range, the Raman spectrum of the MoO_2/MWCNT hybrid shows signals, characteristic of both MoO_2 and MWCNTs. The peak at 1312 cm^{-1} is assigned to the D mode and is attributed to the defects prevalent in the curved graphene sheets in the nanotubes.[28] The peak at 1592 cm^{-1} corresponds to the G band that represents the crystalline structure of the nanotubes.[28] Strong intense peaks are observed at 817 and 990 cm^{-1}, attributable to ν(Mo−O−Mo) and ν(Mo═O) stretching modes of MoO_2, confirming the inclusion of MoO_2 in MWCNTs. The forest-like growth and entangled assembly of MWCNTs is visible from Figure 3c. The images of the MoO_2/MWCNT hybrid reveal the sphere shaped-flower like morphology of MoO_2 nanostructures and these nanostructures are connected by the MWCNTs (Figure 3d, e).

TEM and HRTEM images of the neat MWCNTs, neat MoO_2 and MoO_2/MWCNT hybrid are shown in Figure 4. The neat nanotubes are characterized by curved structures and in general, they have an inner diameter of about 5−8 nm and an outer diameter of about 20 nm (Figure 4a and b). The high-magnification image of the tip shows that the nanotubes have open ends with circular shapes (inset of Figure 4a). The inset of Figure 4b shows the lattice scale image from an individual MWCNT, indicating the high crystallinity of the walls. The walls are composed of graphite sheets aligned parallel to the tube axis. The interwall spacing is about 0.31 nm which is consistent with the standard (well-reported) spacing of about 0.34 nm.[29,30] The flowerlike morphology of MoO_2 is evident from Figure 4c, wherein one large MoO_2 particle comprising petal like shapes is seen. The low magnification image of the MoO_2/MWCNT hybrid (Figure 4d) reveals the spherical flower like shapes of MoO_2 to be connected by the coiled MWCNTs. The diameter of the MoO_2 spheres varies from 50 to 300 nm and in some portions the spheres tend to aggregate and form large particles. But at the nanolevel, the sphere-shaped floral morphology intertwined with MWCNTs is the dominant feature, which is advantageous for electrochemical applications. The MWCNTs being intrinsically electron-conducting in nature, can provide conducting pathways for electron transfer and transport during charging-discharging process. The MoO_2/MWCNT hybrid is therefore expected to show an improved performance in comparison to neat MoO_2 as a Li-ion battery anode due to the presence of uniformly distributed MWCNTs in the MoO_2/MWCNT hybrid. The direct and intimate contact which is established between the MWCNTs and MoO_2 nanoparticles is perceptible from Figure 4e. A high magnification image of the petal like shape of MoO_2 (Figure 4f) shows the petals to be largely composed of elongated-strand like structures. On examining the section of one such petal (Figure 4g), we find that lattice fringes of MoO_2 are oriented in a direction which is almost perpendicular to the growth axis of the MoO_2 petals. The lattice fringes of MoO_2 are not well-resolved in all regions of the MoO_2/MWCNT hybrid, because of some degree of amorphicity in the MoO_2/MWCNT hybrid. A lattice scale image recorded from a defect-free section of the crystalline MoO_2 nanoparticles (Figure 4h) reveals the interplanar spacing to be ~0.32 nm, which augurs well with a d-spacing of 3.42 Å corresponding to the (011) reflection of monoclinic MoO_2, in accordance with the PCPDF NO:

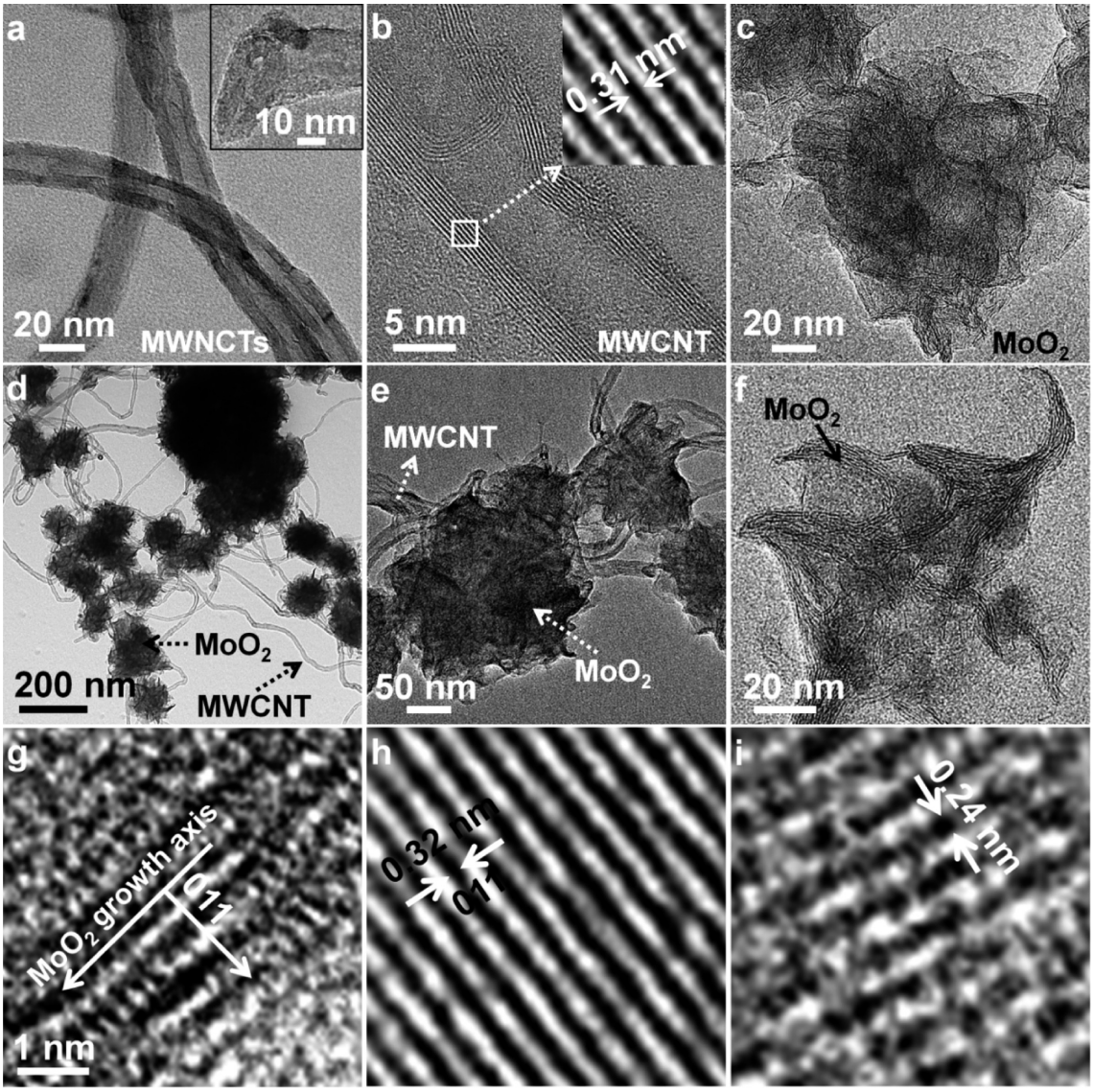

Figure 4. (a) TEM image of neat MWCNTs, inset shows a nanotube end, (b) HRTEM image of a single MWCNT, inset shows the corresponding lattice scale view, (c) flower-like morphology of neat MoO_2, (d) low- and (e) high-magnification images of MoO_2 flowers connected by MWCNTs in the MoO_2/MWCNT hybrid, (f) high magnification image illustrating the MoO_2 petals to be composed of elongated strands, (g) the growth axis of MoO_2 strands is normal to the lattice plane (011), (h) lattice scale image of MoO_2 extracted from the MoO_2/MWCNT hybrid oriented along the (011) plane, and (i) a lattice scale image of a semicrystalline MoO_2 oriented along the (020) plane.

860135. The lattice scale image recorded from another region of the same MoO_2/MWCNT hybrid (Figure 4i) reveals the presence of crystalline particles oriented along the (020) plane of monoclinic MoO_2. Our HRTEM results are in agreement with our XRD findings.

3.2. Growth Mechanism of MoO_2 Flowers. To understand the growth mechanism of MoO_2 flowers, we heated the MoO_2 precursor with fixed amount of AOT of 2 g for different durations 6, 12, and 24 h, while keeping all other experimental parameters constant. The XRD patterns of the products formed after 6, 12, and 24 h hydrothermal treatment correspond to monoclinic MoO_2 (see Figure S1 in the Supporting Information) and peaks from no other impurity phases and side products were observed. At the first stage, when the precursor solution of MoO_2 (AHM dissolved in H_2O) was added to AOT (dissolved in cyclohexane) solution, the MoO_2 precursor moieties are entrapped by the central polar part of the reverse micelles formed by AOT in cyclohexane. During the heat treatment under hydrothermal conditions for 6 h, the MoO_2 precursor moieties in the core of the reverse micelle nucleate and form bundles of stub-shaped particles (Figure 5a). The particle morphology does not alter significantly, when the heating duration was increased to 12 h (Figure 5b). However, when the duration of heating was increased to 24 h, the grain boundaries of the MoO_2 stub like shapes become distinct, they also flatten out and they also coalesce to form small floral shapes, with an average diameter of about 135 nm. On further heating to 36 h, the flaky MoO_2 particles undergo Ostwald ripening and grow into spherical flower shaped nanostructures of around 1000 nm dimensions. Under hydrothermal conditions, the heptamolybdate anions entrapped in the core of the reverse micelle undergo decomposition to form MoO_3 particles which are instantaneously reduced to MoO_2 by the hydrocarbons generated in situ from the decomposition of AOT. We have represented these steps in eqs 1−3.

dx.doi.org/10.1021/am3031536 | ACS Appl. Mater. Interfaces 2013, 5, 2555−2566

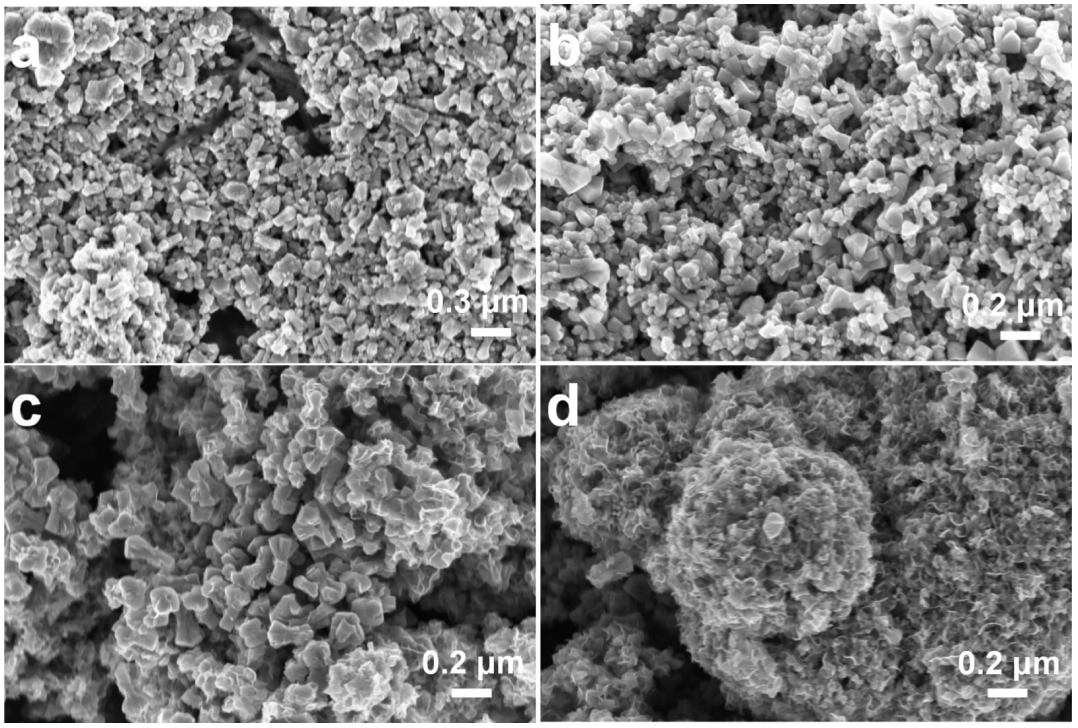

Figure 5. FE-SEM images neat MoO_2 prepared by hydrothermal heating of the precursor containing 2 g AOT for (a) 6, (b) 12, (c) 24, and (d) 36 h, at a fixed temperature of 200 °C.

Scheme 1. Schematic Representation for the Preparation of MoO_2/MWCNT Hybrid

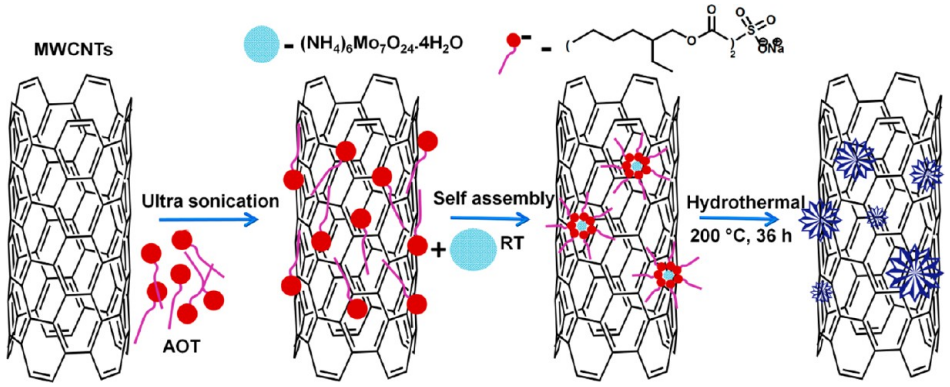

$$(NH_4)_6Mo_7O_{12}\cdot 4H_2O + 3H_2O \rightarrow H_6Mo_7O_{12}\cdot 4H_2O + 6NH_3\uparrow + 3H_2O \quad (1)$$

$$H_6Mo_7O_{12}\cdot 4H_2O \rightarrow 7MoO_3 + 6H_2O \quad (2)$$

$$2MoO_3 + C \rightarrow 2MoO_2 + CO_2 \quad (3)$$

To further increase the electronic conductivity of MoO_2, we used MWCNTs and prepared the MoO_2/MWCNT hybrid. MWCNTs play a critical role in separating the flower-shaped nanostructures and prevent them from aggregating. The mechanism for the formation of flower kind of nanostructures is similar to the above-mentioned process but the whole process now occurs on the surface of the MWCNTs. We have showed these steps in a schematic representation (Scheme 1). In the initial step, we prepared debundled, solubilized, and well-dispersed MWCNTs in ethanol/cyclohexane solution, by addition of AOT. AOT forms reverse micelles in the medium, with the sulfonate groups in the core of the micelle and the alkyl chains face the organic solvent molecules. These negatively charged moieties get adsorbed on the surface of MWCNTs, and prevent the MWCNTs from stacking. Upon subsequent addition of AHM/water solution to the MWCNT/AOT dispersion, the reverse micelles of AOT entrap the heptamolybdate ions via Coulombic repulsion, and attach noncovalently to the surface of MWCNTs. Upon hydrothermal heating for 36 h, the floral-nanostructures of MoO_2 are flanked to the surface of MWCNTs are formed after organic burnout and they remain discrete.

The BET specific surface area of the MoO_2/MWCNT hybrid was obtained by recording nitrogen adsorption−desorption isotherms (Figure 6). The as-prepared MoO_2/MWCNT hybrid shows a specific surface area of 117.5 $m^2\ g^{-1}$ which is higher than that observed for neat MoO_2 (56.9 $m^2\ g^{-1}$). The larger specific surface area of MoO_2/MWCNT hybrid indicates the availability of more number of electro-active sites for Li ion storage. The pore volumes for the two samples were also calculated by using the N_2 sorption isotherm (Figure 6). The

dx.doi.org/10.1021/am3031536 | ACS Appl. Mater. Interfaces 2013, 5, 2555−2566

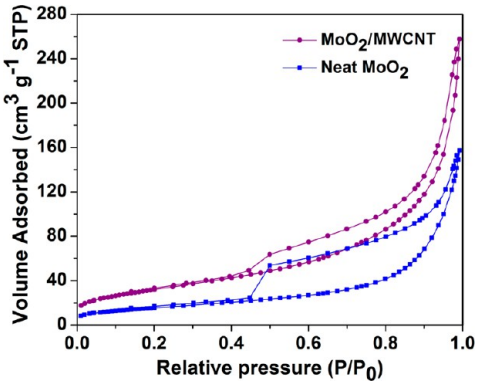

Figure 6. N_2 adsorption/desorption isotherms of neat MoO_2 and the MoO_2/MWCNT hybrid.

pore volume was found to be 0.39 cm^3 g^{-1} for the MoO_2/MWCNT hybrid, whereas the pore volume of neat MoO_2 was 0.24 cm^3 g^{-1}. The higher specific surface area and the larger pore volume of the MoO_2/MWCNT hybrid can also aid in accommodating the volume changes of MoO_2, during charge/discharge cycles, which can lead to better cycling stability.

To determine the chemical composition of the MoO_2/MWCNT hybrid, X-ray photoelectron spectroscopy (XPS) measurements were carried out and are presented in Figure 7. The survey spectrum (Figure 7a) of the MoO_2/MWCNT hybrid shows distinct signals at 230.2, 284.7, 394.6, 412.1, and 530.8 eV which are assigned to the Mo3d, C1s, $Mo3p_{3/2}$, $Mo3p_{1/2}$ and O1s respectively; indicating contributions from both MoO_2 and MWCNT. The C1s signal (Figure 7b) shows an asymmetrical profile owing to the presence of different oxygen containing groups covalently linked to the carbon atoms on MWCNTs. The deconvoluted C1s spectrum shows four components and these are assigned to: C−C bonds at 284.2 eV, C−O groups at 285.2 eV, C═O groups at 286.8 eV and the O−C═O moieties at 288.6 eV. The deconvoluted Mo3d core level spectrum (Figure 7c) shows four peaks; with the lower energy spin−spin doublet due to the +4 oxidation state of the Mo, at 231.7 and 228.4 eV due to $Mo^{IV}3d_{3/2}$ and Mo^{IV} $3d_{5/2}$ species respectively. The higher energy, lower intensity peaks (in comparison to Mo^{IV} peaks) at 233 and 229 eV originate from Mo^{VI} $3d_{3/2}$ and Mo^{VI} $3d_{5/2}$ of MoO_3. Our positions for Mo^{IV} and Mo^{VI} agree well with the reported values for MoO_2.[31] MoO_3 formation occurs due to the slight surface oxidation of metastable MoO_2 in air. The broad O1s core level spectrum could be split into three deconvoluted components; two components at 533.2 and 531.8 eV are attributable to residual oxygen bonded to carbon in MWCNTs, i.e., C−O and C═O groups and the third component at 530.4 eV arises from the Mo−O bonds (Figure 7d).

3.2. Nanoscale Surface Potential Mapping. The work functions of MoO_2 and MoO_2/MWCNT are useful for visualizing the energetics of the Li-ion cell. By KPFM, the topography of sample surface is measured in tapping mode and the surface potential variation is measured with the conducting tip simultaneously. The tip was held at a fixed height of 50 nm above the MoO_2 or MoO_2/MWCNT pellet surface, and it is charged due to the applied ac potential. The sample surface is also charged since it is in the vicinity of the charged tip. As the tip with a known work function (Φ_{tip}) contacts the sample (with the unknown work function, Φ_{sample}) electrically, a potential difference between the tip and the sample is produced. The work function of the sample was deduced using eq 4.

$$V_{CPD} = (\Phi_{tip} - \Phi_{sample})/e \quad (4)$$

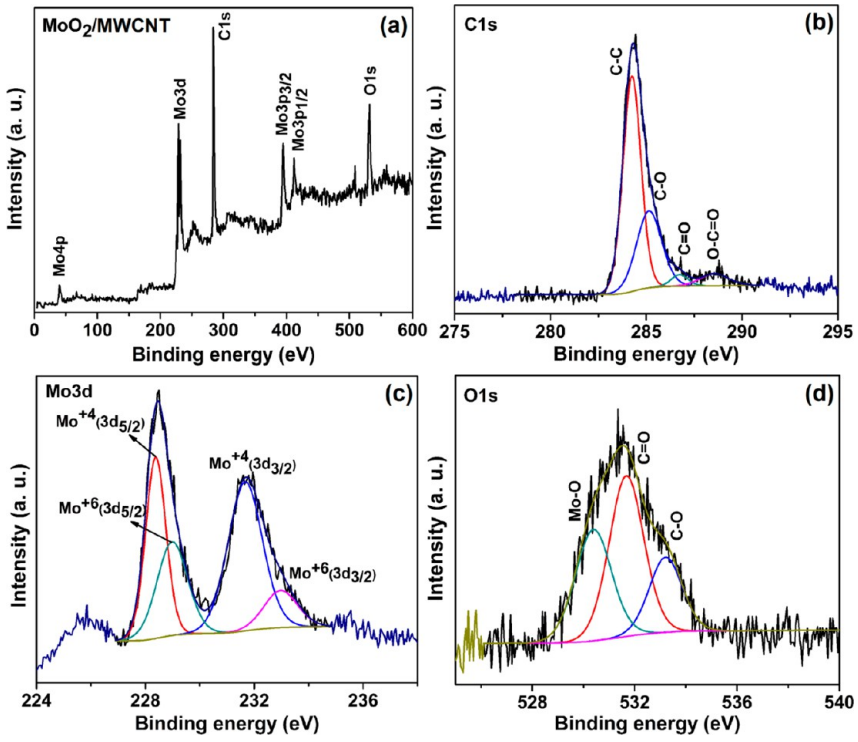

Figure 7. (a) XPS survey spectrum of the MoO_2/MWCNT hybrid and deconvoluted core level spectra of (b) C1s, (c) Mo3d, and (d) O1s of the MoO_2/MWCNT hybrid.

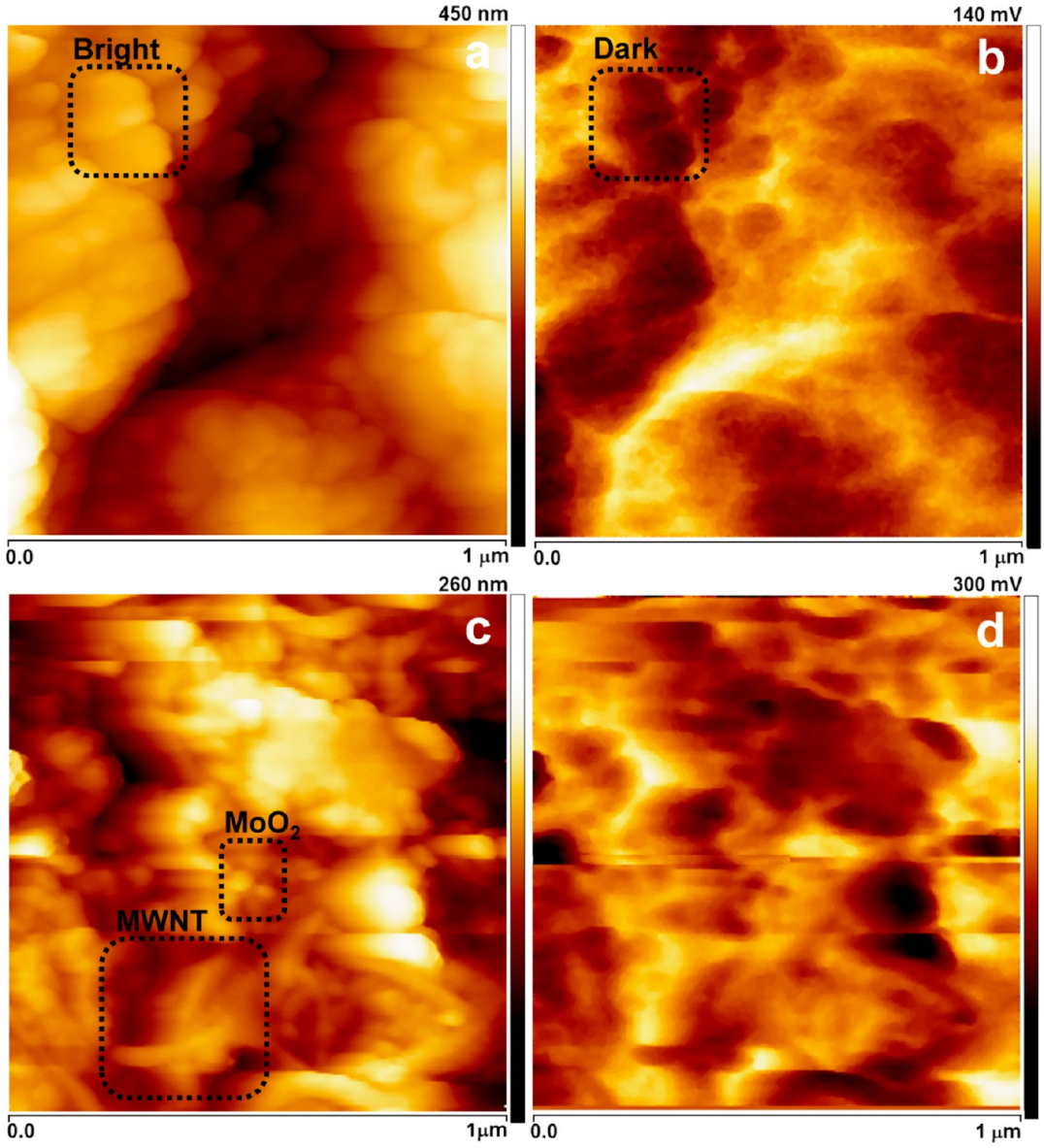

Figure 8. Topography and surface potential maps of (a, b) neat MoO_2 and (c, d) the MoO_2/MWCNT hybrid electrodes recorded over scanned areas of 1 μm × 1 μm. The conducting tip was fixed at a height of 50 nm with respect to sample surface for recording the maps shown in b and d.

The topography and the corresponding surface potential maps of neat MoO_2 and MoO_2/MWCNT hybrid are shown in Figure 8. The cross-sectional profiles and the potential height profiles were also measured along the midsection of each image and these are given in Figure S2 (Supporting Information). The dark domains in the topography images are seen as bright regions in the corresponding surface potential maps for both the samples. The dark domains in the surface potential map are characterized by a lower surface potential as compared to the bright regions in the same map. This can be judged from the color scaling shown on the right sides of the panels showing surface potential variation across scanned areas of 1 μm × 1 μm. The surface potentials (V_{CPD}) of the neat MoO_2 and MoO_2/MWCNT hybrid are 140 and 300 mV respectively (Figure 7b, d) respectively. Using eq 4, the work functions of neat MoO_2 and the MoO_2/MWCNT hybrid were deduced to be 5.36 and 5.2 eV, respectively. Our value for neat MoO_2 is slightly lower than that reported for vacuum deposited MoO_2 (Φ = 5.6 eV), by ultraviolet photoelectron microscope. The work function of MoO_2 broadly lies in the range of 5−6.5 eV, depending upon preparation conditions.[32,33] The work function can be approximated to the Fermi level position in both cases. The Fermi level of neat MoO_2 is poised at 5.36 eV and that of the MoO_2/MWCNT hybrid is positioned at 5.2 eV with respect to the vacuum level. The energy band diagram is shown in Figure 9. The Li-ion battery configuration used for the electrochemical characterization of the neat materials and MoO_2/MWCNT hybrid was as follows: Neat MoO_2 or MoO_2/MWCNT hybrid/$LiPF_6$ in EC/DMC/Li metal. As can be observed from the diagram, the open-circuit voltage (V_{OC}) of the cell is the difference between the Fermi levels or work functions of anode and cathode. The V_{OC} of the cells measured at the beginning of the galvanostatic charge−discharge experiments were 3.05 V (for the cell with neat MoO_2 working as cathode) and 2.9 V (for the cell with MoO_2/MWCNT hybrid as the cathode). The reported value for the work function of lithium metal is 2.4 eV.[34] The V_{OC} of the two cells,

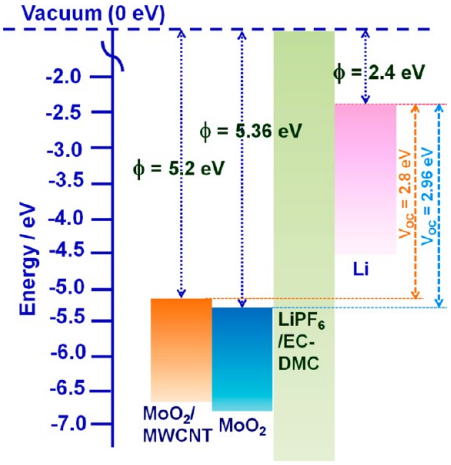

Figure 9. Energy levels for neat MoO_2 and MoO_2/MWCNT electrodes deduced from the surface potential maps.

can be deduced from the values of work function obtained by KPFM using eq 5.

$$V_{OC} = \Phi(\mathrm{MoO_2 or MoO_2/MWCNT}) - \Phi(\mathrm{Li\ metal}) \quad (5)$$

The V_{OC} values for the neat MoO_2 and the MoO_2/MWCNT hybrid were estimated to be 2.96 and 2.8 V, respectively. The V_{OC} values determined from KPFM are quite close to the directly measured values, indicating that the nanoscale surface potential variations mapped by KPFM across the surface of the MoO_2 or the MoO_2/MWCNT hybrid are reliable. It is apparent that the work function of MoO_2 (Φ = 5.36 eV) is lowered upon incorporation of MWCNTs as for the MoO_2/MWCNT hybrid, Φ = 5.2 eV. A similar decrease in work function from 6.5 eV to about 5.5 eV has been reported in past for conducting MoO_2, as a function of increasing SiO_2:Mo ratio from 0 to 33%.[33] Lower the work function of the anode material (as observed for the MoO_2/MWCNT hybrid in comparison to neat MoO_2), greater would be the ease of oxidation, as lesser energy would be required to remove an electron from the material with a lower work function. Our surface potential studies clearly show that the surface potential profile of the MoO_2/MWCNT hybrid renders it more suitable for Li-ion battery applications as compared to the neat oxide.

3.3. Electrochemical Characteristics. Before measuring the electrochemical performance, the amount of MWCNT in the MoO_2/MWCNT hybrid was estimated by performing thermo gravimetric analysis (TGA) and differential thermal analysis (DTA) in air flow in the range of 30 to 900 °C. Figure S3 in the Supporting Information shows the TG/DTA curves of neat MWCNTs and the MoO_2/MWCNT hybrid. The MWCNT content in the MoO_2/MWCNT hybrid was deduced to be ~17.5%.

The lithium storage performance of the MoO_2/MWCNT hybrid and neat MoO_2 were measured by CV and galvanostatic charge−discharge experiments. Cyclic voltammograms of the MoO_2/MWCNT hybrid recorded at scan rates of 0.05 and 0.1 mV s^{-1}, respectively, are displayed in Figure 10a and b. An irreversible peak observed in the first cycle at 0.45 V during the cathodic discharge, is attributed to the conversion reaction of MoO_2[35] and reduction of solution species to form a passivating film on the anode surface.[13,15,36] In the following cycles, two redox couples located around 1.74/2.37 V and 1.21/1.68 V are observed which are due to the phase transitions of the partially lithiated Li_xMoO_2 during lithium insertion and extraction.[37,12−15] The CV profiles of the MoO_2/MWCNT hybrid remain steady with cycling whereas the area under the CV curves of neat MoO_2 (see Figure S4 in the Supporting Information) decreased with cycling, indicating excellent cycling stability of the MoO_2/MWCNT hybrid compared to MoO_2. The galvanostatic charge−discharge curves of the MoO_2/MWCNT hybrid measured at a current density of 100

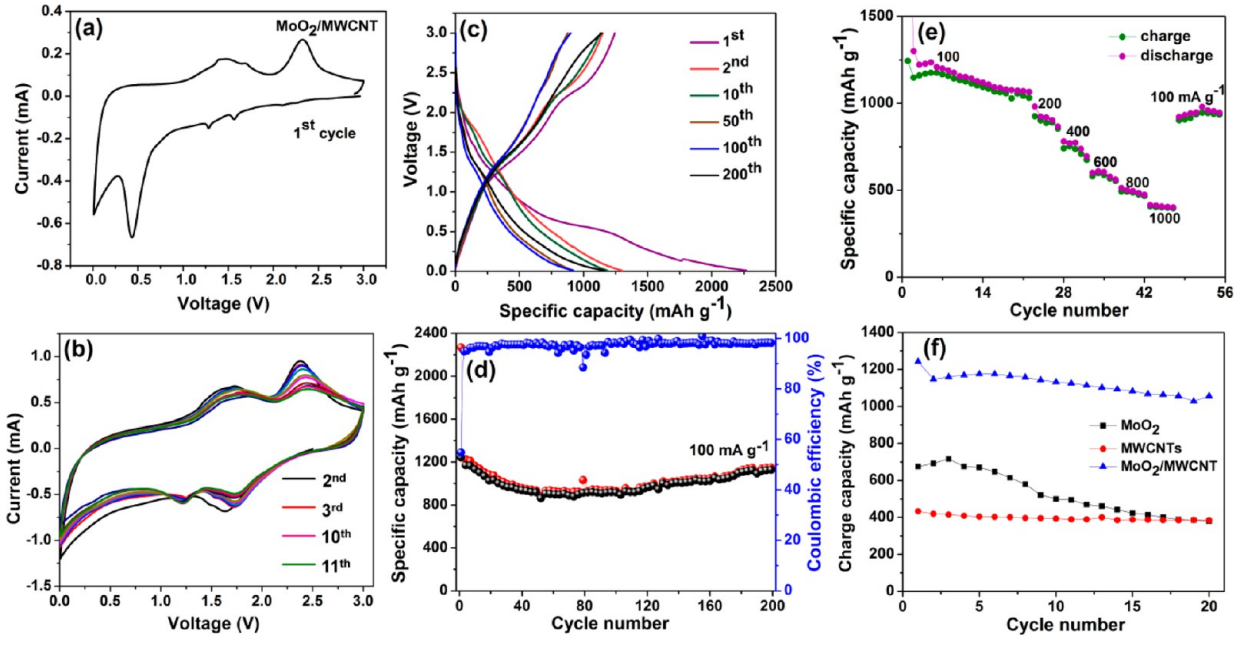

Figure 10. Cyclic voltammograms of the MoO_2/MWCNT hybrid at scan rates of (a) 0.05 and (b) 0.1 mV s^{-1} in the potential range of 0 to 3 V, (c) galvanostatic charge−discharge curves and (d) cyclability and Coulombic efficiency of the MoO_2/MWCNT hybrid at a current density of 100 mA g^{-1} and (e) rate capability of the MoO_2/MWCNT hybrid and (f) cyclabilities of neat MoO_2, neat MWCNTs and MoO_2/MWCNT hybrid at a current density of 100 mA g^{-1}.

dx.doi.org/10.1021/am3031536 | ACS Appl. Mater. Interfaces 2013, 5, 2555−2566

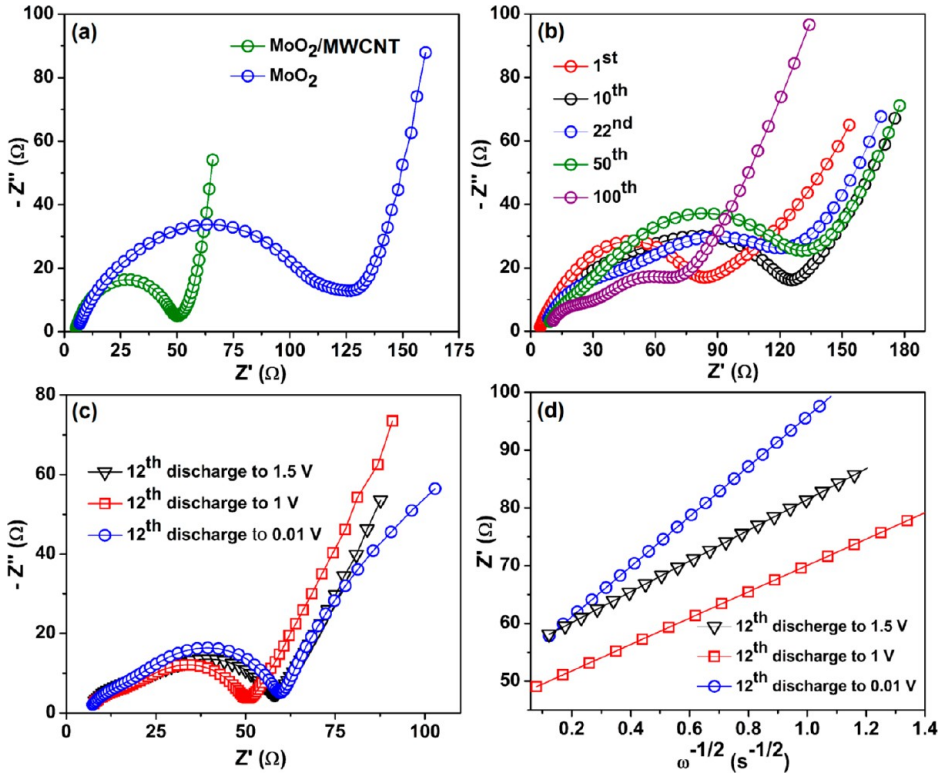

Figure 11. (a) Comparison of Nyqvist plots of neat MoO_2 with the MoO_2/MWCNT hybrid, (b) Nyqvist plots recorded intermittently during charge−discharge cycles of the MoO_2/MWCNT hybrid (c) Nyqvist plots at 1.5, 1, and 0.01 V during the 12th discharge (d) Z' versus $\omega^{-1/2}$ curves in the low frequency region of the MoO_2/MWCNT hybrid.

mA g^{-1} and in the voltage range of 0.01 to 3 V are shown in Figure 10c. In the first cycle, two discharge plateaus at ∼1.6/1.2 V and two charge plateaus around 1.5/2.2 V were observed; these plateaus are reversible in the subsequent cycles. These results agree well with the CV results. The first discharge and charge capacities were deduced to be 2270 and 1243 mA h g^{-1}, respectively, with 55% Coulombic efficiency (comparison of theoretical and obtained specific capacities is provided in the Supporting Information). The irreversible capacity loss in the first cycle is inevitable for most of the transition metal oxides and according to previous reports,[6,16,17] it is due to the formation of solid electrolyte interface and electrolyte degradation. Figure 10d shows the cyclability and Coulombic efficiency of MoO_2/MWCNT hybrid observed at a current density of 100 mA g^{-1}. The MoO_2/MWCNT hybrid show excellent cycling stability for the measured 200 cycles. After 200 cycles, discharge and charge capacities are 1151.3 and 1143.7 mA h g^{-1}, respectively, with ∼99% Coulombic efficiency. After 200 cycles it retained 92% capacity of the initial cycle. Our values are comparable to those achieved in some of the earlier reports on MoO_2/C composite, MoO_3 nanobelts, and MoO_3 nanorods.[38−40] For the complete reduction of Mo (IV) to Mo (0), a maximum specific capacity of 840 mA h g^{-1} is expected, as per the following equation.

$$MoO_2 + 4Li^+ + 4e^- \leftrightarrows Mo + 2Li_2O \quad (6)$$

The very high capacity achieved for the MoO_2/MWCNT hybrid is due to the synergy between MoO_2 flower-like nanostructures and MWCNTs (more details are provided in the Supporting Information). In the MoO_2/MWCNT hybrid, the flowerlike shapes of MoO_2 and the tubular structures of MWCNTs account for the high specific area, which increases the ability for Li ion uptake, and the fact that the MoO_2 flowers and the MWCNTs are directly connected, enhances the ability of the electrode to conduct electrons, as MWCNTs are intrinsic electron conductors. Furthermore, the MWCNTs prevent the MoO_2 particles from aggregating and the MoO_2 flowers also inhibit the nanotubes from bundling up. The FE-SEM images of the MoO_2/MWCNT hybrid after 100 cycles measured at a current density of 100 mA g^{-1} are shown in Figure S5 (Supporting Information). The FE-SEM images show that after 100 cycles, the flowerlike nanostructures are retained but they seem to be composed of interconnected needlelike shapes separated by pores; the overall topology is different from that of the as-fabricated MoO_2/MWCNT hybrid, possibly due to solid electrolyte interphase formation in the cycled sample. The MoO_2/MWCNT hybrid also showed a good rate performance. The capacity was as high as 408 mA h g^{-1} even upon increasing the current density by 10 times. At the end of 55 cycles, a capacity of ∼935 mA h g^{-1} at a current density of 100 mA g^{-1} was retained even after several charge discharge cycles at various current densities (Figure 10e), indicating the high rate capability and good cycling stability. The effect of MWCNTs on MoO_2 was further explained by comparing the cycling behavior of neat MoO_2 (discharge−charge curves shown in Figure S6 in the Supporting Information), neat MWCNTs and the MoO_2/MWCNT hybrid at 100 mA g^{-1} current density (Figure 10f). Neat MoO_2 exhibits an initial reversible capacity of ∼674.8 mA h g^{-1} and with increasing cycles the capacity fades drastically and after 20 cycles, the capacity reduced to only 380 mA h g^{-1}. On the other hand, neat MWCNTs exhibit an initial capacity 433.5 mAh g^{-1} and the capacity was almost stable for the measured 20 cycles. Ex situ XRD patterns for the neat MoO_2 and MoO_2/MWCNT hybrid in the intermittent

cycles are shown in Figure S7 (Supporting Information). After first cycle, the MoO_2/MWCNT hybrid retains its crystal structure but peak intensities are reduced and a new peak was seen at 1.5165 Å, which could not be assigned. Upon further increase in number of cycles (5 to 10 to 30), the MoO_2/MWCNT hybrid becomes completely amorphous. On the other hand the ex situ XRD patterns of neat MoO_2 even after 10 cycles shows peaks from Li_xMoO_2, which gives indirect evidence that neat MoO_2 does not undergo complete conversion reaction. This is also one of the reasons for the observed very high capacity of the MoO_2/MWCNT hybrid (more discussion can be found in the Supporting Information). The cycling stability and rate capability of the MoO_2/MWCNT hybrid were further explained by EIS.

EIS spectra were recorded in the initial and intermittent cycling stages and these are presented in Figure 11. The plots show one semicircle followed by a straight line with a slant; the latter is limited to only the low frequency region. The semicircle is attributed to a parallel combination of charge transfer resistance (R_{CT}) and electrical double layer capacitance (C_{dl}), and the straight line stems from the diffusion of charged species through the bulk of the electrode material. Nyqvist plots of the MoO_2/MWCNT hybrid and neat MoO_2 are shown in Figure 11a. The as-fabricated cell of MoO_2/MWCNT hybrid exhibits a lower charge-transfer resistance as compared to neat MoO_2, indicating that the MWCNTs act as efficient charge carriers and facilitate charge transfer at the interface which can lead to higher capacity as observed herein. The Z'' versus Z' curves for the MoO_2/MWCNT hybrid, recorded at intermittent stages of charge/discharge cycling are shown in Figure 11b. From the first cycle to 100th cycle, there is no observable change in charge transfer resistance, which implies that the MoO_2/MWCNT hybrid show a good cycling stability. The diffusion coefficient of lithium ion (Li^+) was determined for the MoO_2/MWCNT hybrid during the 12th discharged state (to 1.5, 1, and 0.01 V, Figure 11c) by using the following equation.

$$D = R^2T^2/2n^4F^4A^2C^2\sigma^2 \quad (7)$$

In eq 7, R is the universal gas constant, T is the absolute temperature, n is the number of electrons involved in the oxidation/reduction per molecule, F is the faraday constant, A is the surface area of the electrode, C is the bulk concentration of lithium ions and σ is the Warburg factor . The value of σ was deduced from the slope of the linear dependence Z' (Ω) versus $\omega^{-1/2}$ plots (Figure 11d) by restricting to only the low frequency region. From eq 4, the $D_{Li}{}^+$ value after discharge to 1.5 V, for the 12th cycle, is 2.43×10^{-11} cm^2 s^{-1}. On further discharging the cell to 1.0 V, the MoO_2/MWCNT hybrid exhibited a D value of 3.31×10^{-11} cm^2 s^{-1}. Upon further discharge to 0.01 V, a $D_{Li}{}^+$ of 9.2×10^{-12} cm^2 s^{-1} was obtained. For neat MoO_2, for the eighth discharge to 1.0 V (see Figure S8 in the Supporting Information), a $D_{Li}{}^+$ of 4.18×10^{-14} cm^2 s^{-1} was observed, which is 2 orders of magnitude lower than that of the MoO_2/MWCNT hybrid. It is evident that the MoO_2/MWCNT hybrid has a microstructure which is more conducive for Li-ion transport as compared to the neat oxide and is therefore a promising candidate for anodes in practical Li-ion batteries.

4. CONCLUSION

A MoO_2/MWCNT hybrid composed of spherical floral nanostructures of MoO_2, interlinked with curved MWCNTs has been synthesized by a hydrothermal route. The formation of MoO_2 flower-like shapes is dictated by the surfactant, AOT. The unique nanoscale architecture of the MoO_2/MWCNT hybrid is responsible for a large reversible electrochemical lithium storage capacity of 1025.2 mA h g^{-1} achieved at a current density of 100 mA g^{-1} after 160 cycles in comparison to a much lower value of 220 mA h g^{-1} (after 20 cycles) obtained for neat MoO_2. The inherent electron conducting nature of MWCNTs enables efficient electron transfer and transport in the MoO_2/MWCNT hybrid by the virtue of the direct interconnects formed between MoO_2 flowers and MWCNTs. The increased electrochemical activity of the MoO_2/MWCNT hybrid is also attributed to a lower nanoscale work function relative to neat MoO_2, which renders the oxidation of the MoO_2/MWCNT hybrid easier, as compared to neat MoO_2. The unusual topology of the MoO_2/MWCNT hybrid, the high rate capability (as it shows a capacity of 408 mA h g^{-1} at a high current density of 1000 mA g^{-1}) and the excellent cyclability demonstrate its' utilitarian value as a high performance anode in Li-ion batteries. Our simple single step approach for fabricating a MoO_2/MWCNT hybrid shows that this strategy can be applied to other oxides as well to yield unique architectures for Li-ion battery anodes.

■ ASSOCIATED CONTENT

Ⓢ Supporting Information

XRD patterns of neat MoO_2, KPFM details and cross-sectional profiles for neat MoO_2 and MoO_2/MWCNT hybrid, TG/DTA curves for neat MWCNTs and MoO_2/MWCNT hybrid, CV curves of neat MoO_2, FE-SEM images of cycled MoO_2/MWCNT hybrid, charge−discharge curves of neat MoO_2, ex situ XRD patterns of neat MoO_2 and MoO_2/MWCNT hybrid, EIS plots of neat MoO_2 and additional discussion. This material is available free of charge via the Internet at http://pubs.acs.org.

■ AUTHOR INFORMATION

Corresponding Author

*E-mail: mdeepa@iith.ac.in. Tel: +91-40-23016024.

Notes

The authors declare no competing financial interest.

■ ACKNOWLEDGMENTS

We thank International Advanced Research Centre for Powder Metallurgy and New Materials (ARCI) and Indo-French Centre for the Promotion of Advanced Research (CEFIPRA) for financial support.

■ REFERENCES

(1) Tarascon, J. M.; Armand, M. *Nature* **2001**, *414*, 359−367.
(2) Arico, A. S.; Bruce, P.; Scrosati, B.; Tarascon, J. M.; Schalkwijk, W. V. *Nat. Mater.* **2005**, *4*, 366−377.
(3) Bruce, P. G.; Scrosati, B.; Tarascon, J. M. *Angew. Chem., Int. Ed.* **2008**, *47*, 2930−2946.
(4) Kambe, N.; Dresselhaus, M. S.; Dresselhaus, G.; Basu, S.; McGhie, A. R.; Fischer, J. E. *Mater. Sci. Eng.* **1979**, *40*, 1−4.
(5) Guo, K.; Pan, Q.; Fang, S. *J. Power Sources* **2002**, *111*, 350−356.
(6) Poizot, P.; Laruelle, S.; Grugeon, S.; Dupont, L.; Tarascon, J. M. *Nature* **2000**, *407*, 496−499.
(7) Caban, J.; Monconduit, L.; Larcher, D.; Palacín, M. R. *Adv. Mater.* **2010**, *22*, E170−E192.
(8) Lee, K. T.; Cho, J. *Nano Today* **2011**, *6*, 28−41.
(9) Li, H.; Zhou, H. *Chem. Commun.* **2012**, *48*, 1201−1217.
(10) Wang, H.; Cui, L. F.; Yang, Y.; Casalongue, H. S.; J. T. Robinson, J. T.; Liang, Y.; Cui, Y.; Dai, H. *J. Am. Chem. Soc.* **2010**, *132*, 13978−13980.

(11) Xia, H.; Lai, M.; Lu, L. *J. Mater. Chem.* **2010**, *20*, 6896−6902.
(12) Shi, Y.; Guo, B.; Corr, S. A.; Shi, Q.; Hu, Y. S.; Heier, K. R.; Chen, L.; Seshadri, R.; Stucky, G. D. *Nano Lett.* **2009**, *9*, 4215−4220.
(13) Gao, Q.; Yang, L.; Lu, X.; Mao, J.; Zhang, Y.; Wu, Y.; Tang, Y. *J. Mater. Chem.* **2010**, *20*, 2807−2812.
(14) Guo, B.; Fang, X.; Li, B.; Shi, Y.; Ouyang, C.; Hu, Y. S.; Wang, Z.; Stucky, G. D.; Chen, L. *Chem. Mater.* **2012**, *24*, 457−463.
(15) Yang, L. C.; Gao, Q. S.; Zhang, Y. H.; Tang, Y.; Wu, Y. P. *Electrochem. Commun.* **2008**, *10*, 118−122.
(16) Zhou, L.; Bin Wu, H.; Wang, Z.; Lou, X. W. *ACS Appl. Mater. Interfaces* **2011**, *3*, 4853−4857.
(17) Sun, Y.; Hu, X.; Luo, W.; Huang, Y. *J. Mater. Chem.* **2012**, *22*, 425−431.
(18) Ji, X.; Herle, P. S.; Rho, Y.; Nazar, L. F. *Chem. Mater.* **2007**, *19*, 374−383.
(19) Bhaskar, A.; Deepa, M.; Rao, T. N.; Varadaraju, U. V. *J. Power Sources* **2012**, *216*, 169−178.
(20) Sun, Y.; Hu, X.; Luo, W.; Huang, Y. *ACS Nano* **2011**, *5*, 7100−7107.
(21) Xu, Y.; Yi, R.; Yuan, B.; Wu, X. F.; Dunwell, M.; Lin, Q. L.; Fei, L.; Deng, S. G.; Andersen, P.; Wang, D. H.; Luo, H. M. *J. Phys. Chem. Lett.* **2012**, *3*, 309−314.
(22) Iijima, S. *Nature* **1991**, *354*, 56−58.
(23) Balasubramanian, K.; Burghard, M. *Small* **2005**, *1*, 180−192.
(24) Wang, S. C.; Yang, H.; Banerjee, S.; Herman, I. P.; Akins, D. L. *Mater. Lett.* **2008**, *62*, 843−845.
(25) Islam, M. F.; Rojas, E.; Bergey, D. M.; Johnson, A. T.; Yodh, A. G. *Nano Lett.* **2003**, *3*, 269−273.
(26) Rastogi, R.; Kaushal, R.; Tripathi, S. K.; Sharma, A. L.; Kaur, I.; Bharadwaj, L. M. *J. Colloid Interface Sci.* **2008**, *328*, 421−428.
(27) Bai, Y.; Park, I. S.; Lee, S. J.; Wen, P. S.; Bae, T. S.; Lee, M. H. *Colloids Surf., B* **2012**, *89*, 101−107.
(28) Masarapu, C.; Subramanian, V.; Zhu, H.; Wei, B. *Adv. Funct. Mater.* **2009**, *19*, 1008−1014.
(29) Baskaran, D.; Mays, J. W.; Bratcher, M. S. *Angew. Chem., Int. Ed.* **2004**, *43*, 2138−2142.
(30) Xu, Z.; Wang, L.; Zheng, Q. *Small* **2008**, *4*, 733−737.
(31) Zhao, X.; Cao, M.; Liu, B.; Tiana, Y.; Hu, C. *J. Mater. Chem.* **2012**, *22*, 13334−13340.
(32) Matsushima, T.; Adachi, C. *J. Appl. Phys.* **2008**, *103*, 034501−4.
(33) Liang, Y.; Tracy, C.; Weisbrod, E.; Fejes, P.; Theodore, N. D. *Appl. Phys. Lett.* **2006**, *88*, 081901−3.
(34) Anderson, P. A. *Phys. Rev.* **1949**, *75*, 1205−1207.
(35) Jung, Y. S.; Lee, S.; Ahn, D.; Dillon, A. C.; Lee, S. H. *J. Power Sources* **2009**, *188*, 286−291.
(36) Sun, Y.; Hu, X.; Yu, J. C.; Li, Q.; Luo, W.; Yuan, L.; Zhanga, W.; Huang, Y. *Energy Environ. Sci.* **2011**, *4*, 2870−2877.
(37) Dahn, J. R.; McKinnon, W. R. *Solid State Ionics* **1987**, *23*, l−7.
(38) Wang, Z.; Chen, J. S.; Zhu, T.; Madhavi, S.; Lou, X. W. *Chem. Commun.* **2010**, *46*, 6906−6908.
(39) Chen, J. S.; Cheah, Y. L.; Madhavi, S.; Lou, X. W. *J. Phys. Chem. C* **2010**, *114*, 8675−8678.
(40) Wang, Z.; Madhavi, S.; Lou, X. W. *J. Phys. Chem. C* **2012**, *116*, 12508−12513.